Geophysical Research Letters

RESEARCH LETTER
10.1029/2022GL100912

Key Points:

- Time History of Events and Macroscale Interactions during Substorms all-sky imager observations are used across Canada and Alaska for first ever 2D data-informed heat flux estimation
- Data from substorm case study is coupled to SuperThermal Electron Transport model for the heat flux estimation
- Time resolution of energy flux and mean energy inputs shown to be remarkably important in heat flux calculation

Supporting Information:

Supporting Information may be found in the online version of this article.

Correspondence to:

G. V. Khazanov,
George.V.Khazanov@nasa.gov

Citation:

Khazanov, G. V., Gabrielse, C., Glocer, A., Chu, M., Nishimura, Y., & Reyes, P. (2022). A 2D kaleidoscope of electron heat fluxes driven by auroral electron precipitation. *Geophysical Research Letters*, *49*, e2022GL100912. https://doi.org/10.1029/2022GL100912

Received 18 AUG 2022
Accepted 7 SEP 2022

Author Contributions:

Data curation: Christine Gabrielse, Pablo Reyes
Formal analysis: Christine Gabrielse
Methodology: Christine Gabrielse
Software: Alex Glocer, Mike Chu
Visualization: Mike Chu
Writing – original draft: Christine Gabrielse

A 2D Kaleidoscope of Electron Heat Fluxes Driven by Auroral Electron Precipitation

George V. Khazanov[1], Christine Gabrielse[2], Alex Glocer[1], Mike Chu[3], Yukitoshi Nishimura[4], and Pablo Reyes[5]

[1]NASA Goddard Space Flight Center, Greenbelt, MD, USA, [2]The Aerospace Corporation, El Segundo, CA, USA, [3]The Space Weather Lab, George Mason University, Fairfax, VA, USA, [4]Department of Electrical and Computer Engineering and Center for Space Physics, Boston University, Boston, MA, USA, [5]SRI, Menlo Park, CA, USA

Abstract Electron heat flux is an important value for ionospheric space weather modeling networks. Utilizing the 2D array of Time History of Events and Macroscale Interactions during Substorms all-sky-imager (ASI) observations, Gabrielse et al. (2021, https://doi.org/10.3389/fphy.2021.744298) described a new method that estimates the auroral scale sizes of intense precipitating electron energy fluxes and their mean energies during two substorms on 16 February 2010. These parameters in combination with SuperThermal Electron Transport code were used to develop a new methodology to calculate electron thermal fluxes from data inputs in 2D during one of the substorms at 09:40:00 UT across Canada and Alaska. To test the effect of various precipitation lifetimes on electron heat flux values, boxcar averages ranging from 0 to 900 s were applied to the ASI data. These data are then combined with the newly developed kinetic simulation to determine the thermal fluxes associated with the observed diffuse and discrete precipitation.

Plain Language Summary Knowing the thermal electron heat flux at the upper ionospheric boundaries is the *Achilles' heel* of all ionospheric models. Such a thermal heat flux setting is especially difficult to justify in the region of the diffuse aurora that is connected to a large energy reservoir of electrons with energies of a few kiloelectron volts, the Earth's plasma sheet, where MI coupling processes are strongly interconnected. Utilizing the 2D array of Time History of Events and Macroscale Interactions during Substorms all-sky-imager white light observations, Gabrielse et al. (2021, https://doi.org/10.3389/fphy.2021.744298) described a new method that estimates the auroral scale sizes of intense precipitating electron energy fluxes and their mean energies during two substorms. These data are used as inputs to a numerical simulation to determine the thermal fluxes associated with the observed diffuse and discrete precipitation across Canada and Alaska. This is the first-time data in two dimensions are used to inform a model in order to obtain the thermal electron heat flux values. The new method is an improvement over current calculations, since thermal electron heat fluxes cannot be observed directly and thus far have remained elusive and dependent on modeling assumptions.

1. Introduction

The electron thermal fluxes that come from magnetospheric altitudes are important parameters that are required in all global ionospheric models that run in a restricted altitudinal range (Bekerat et al., 2007; Glocer et al., 2012; Richmond et al., 1992; Ridley et al., 2006; Schunk et al., 1986). These electron thermal fluxes define the electron temperature, Te, profile at the upper ionospheric altitudes (and even near the maximum electron density of the F2 region (Fallen & Watkins, 2013)), and, as a result, the total electron density content that is required for different kinds of space weather applications.

These electron heat fluxes (also called thermal fluxes) are carried by electrons with energies below 1 eV, and they must be clearly distinguished from the electron precipitation phenomena that are affiliated with energetic electrons with energies in the range of 100 eV to several keV. These high energy electrons are also of magnetospheric origin, but are formed differently (Khazanov et al., 2020, 2021a). To distinguish these two electron populations in the analysis presented below, we use "precipitation electron fluxes" referring to the high energy electrons and "heat/thermal electron fluxes" referring to the low energy electron fluxes that is the major focus of this study.

Knowledge of electron heat fluxes is especially important in the high latitude auroral region, where magnetic field lines connect the ionosphere with a very large energy reservoir: Earth's plasma sheet. Because the electron heat fluxes are produced by many different magnetospheric processes (Khazanov, 2010; Khazanov

Writing – review & editing: Christine Gabrielse, Alex Glocer, Yukitoshi Nishimura

et al., 2020; Mishin & Streltsov, 2019), this phenomenon has regional variation and strongly depends on the magnetospheric conditions that are affiliated with magnetic storms and substorms. Electron heat flux can't be measured by any space plasma observations because it is carried by electrons with energies below 1 eV. The new methodology that combines data and modeling that we present in this paper offers a novel approach to determining the heat flux, specifically in short duration event studies that cannot rely on long-duration, global averages.

To demonstrate the regional/mesoscale dynamics, motivated by recent studies by Nishimura et al. (2021) and Gabrielse et al. (2021) on estimating precipitating electron energy flux and average energy in aurora from THEMIS All-Sky-Imagers, we selected the data from Gabrielse et al. (2021) for our analysis as a representative case study for the electron heat flux in the auroral region. This data was combined with the newly developed STET based code and systematically applied for the auroral event during one of the substorms at 09:40:00 UT across Canada and Alaska. 09:40:00 UT was chosen because Figure 8 in Gabrielse et al. (2021) displays the conductance calculated from the energy flux and mean energies at this time, for reference. The heat flux in the auroral oval strongly depends on the time history of electron precipitation, and thus it is crucial to obtain event-specific electron precipitation information from observations. Statistical modeling of precipitation would substantially underestimate the precipitation's time variation. This study uses electron precipitation from all-sky imagers as an input for simulating the heat flux.

Most of the auroral energy comes from the precipitating electron fluxes (Newell et al., 2009). That is why in the calculation of electron thermal fluxes we use the theoretical framework that is provided in our recent STET code-based studies for the regions of diffuse (Khazanov et al., 2020) and discrete (Khazanov et al., 2021a) auroras. Both afore mentioned studies have been validated. The STET model has been validated with DMSP (Khazanov et al. (2021a) and FAST (Khazanov et al., 2016) electron spectra measurements as well with optical observation by (Samara et al., 2017). The new technique developed by Gabrielse et al. (2021) was independently validated using Poker Flat Incoherent Scatter Radar (PFISR) data.

2. THEMIS Energy Flux and Mean Energy Inputs

To calculate heat flux, the energy flux and mean energy of the precipitating population must be provided. These can be estimated by THEMIS white light all-sky-imagers. These data were produced by Gabrielse et al. (2021) to determine the relative role that mesoscale auroral features play in the total energy flux precipitated during substorms. They found that mesoscales are very important, contributing up to 80% of the total energy flux during the substorm expansion phase. Their method converted white light intensity to red, green, and blue intensities by calibrating the ASI data to NORSTAR meridian scanning photometer (MSP) data at the same location and time. They used a look-up table to convert color ratios to energy flux and mean energy created from the Boltzmann Three Constituent (B3C) auroral transport code (Strickland et al., 1976, 1993) for the solar wind and geomagnetic parameters of their event (2010-02-16). The thermal heat flux does not generally create strong emission, and thus the products from the all-sky imager data do not include contributions from thermal electrons.

To validate the method, they compared the color intensities, energy fluxes, and mean energies determined from the ASI to those determined by the MSP. They also calculated the Hall conductance with B3C using the ASI inputs and compared to values determined by PFISR. The median percent difference between the ASI and PFISR Hall conductance was 24.2% during discrete aurora and 18.1% during diffuse aurora. Such percent differences provide a sense of confidence in the results, though future work that envelops TREx data (e.g., Gillies et al., 2020) maybe improved further.

In this initial study, we use a mosaic of energy fluxes and mean energies provided by THEMIS at 09:40 UT. Gabrielse et al. (2021) displayed the 2D Hall conductance for this time in their Figure 8e, which is when a discrete aurora was just moving over Poker Flat. How the energy fluxes and mean energies are used to calculate the electron thermal heat flux is described in Section 3.

Because the heat flux value depends on the conditions leading up to the time of interest, we performed boxcar averages over time of the THEMIS energy fluxes and mean energies and assumed constant values for the duration of the average (run for 60, 180, 300, 600, and 900 s). An example of the boxcar averages applied to the data at

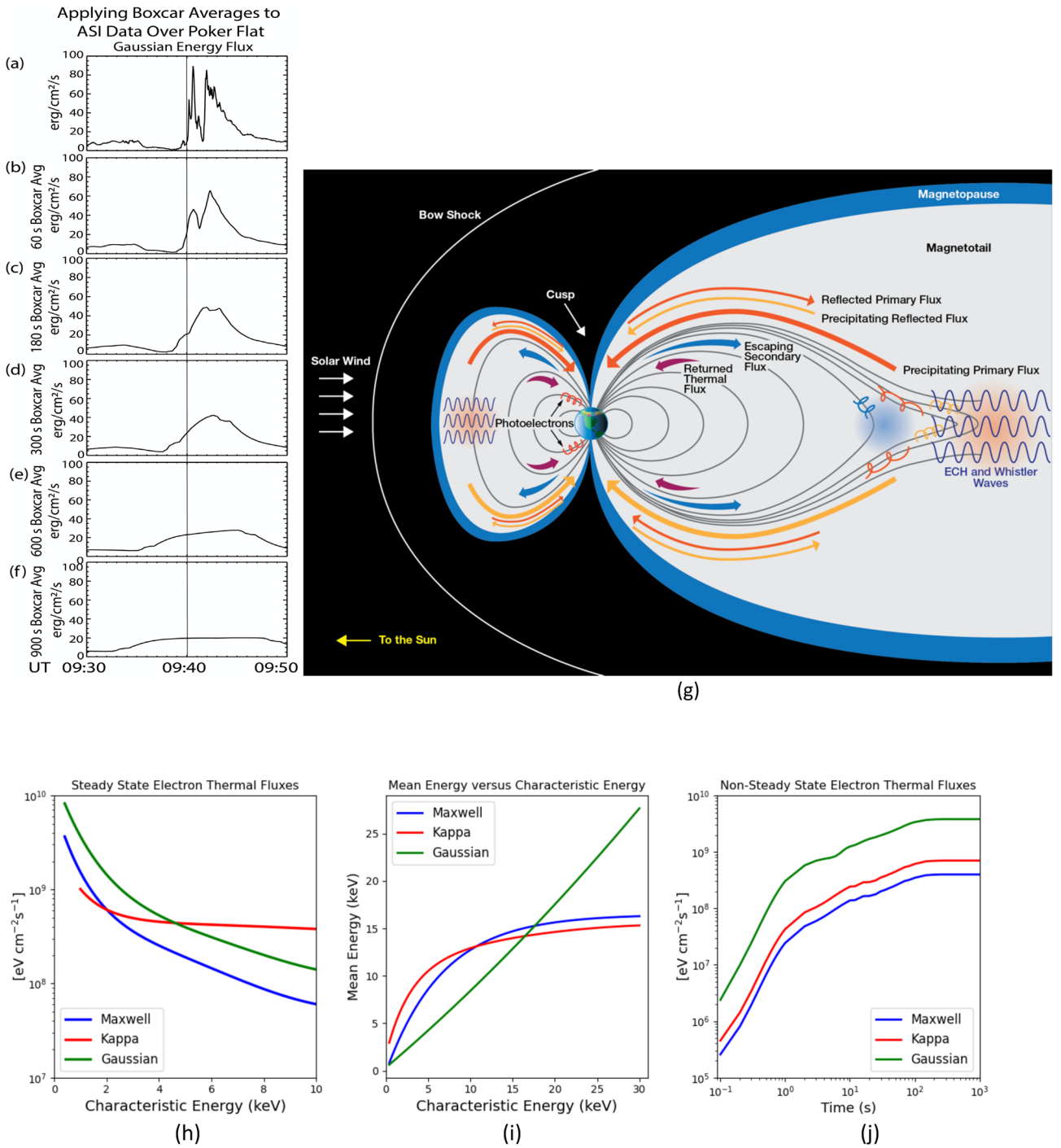

Figure 1. An example of the energy fluxes above Poker Flat from 09:30 to 09:50 UT on 16 February 2010. Vertical lines are drawn at 09:40 UT, which is the time that was used for the heat flux calculation. Each row applies a temporal boxcar average to the data in (a) for different time windows: (b) 60 s, (c) 180 s, (d) 300 s, (e) 600 s, (f) 900 s. This boxcar average was applied to all locations covered by the THEMIS ASIs in order to produce the first two columns in Figures 2 and 3. Electron heat flux formation processes: (g) MI energy interplay that produces electron heat fluxes (adapted from Khazanov et al., 2020); (h) Electron thermal fluxes dependence on characteristic energy of precipitated electrons that are described by different electron distributions of Equation 1–3; (i) Connections between characteristics and mean energies; and (j) time dependent electron thermal fluxes development as function of different electron precipitated electrons distributions of Equation 1–3.

the Poker Flat location is included in Figures 1a–1f. The boxcar average of the mean energy was weighted by the precipitated energy flux, to provide weight to those populations with greater fluxes:

$$\text{Boxcar Average of Mean Energy} = \frac{\sum_{i=-b/2}^{b/2}(W_i J_i)}{\sum_{i=-b/2}^{b/2}(J_i)} \quad (1)$$

Where W_i = mean energy at time i, J_i = energy flux at time i, and b = boxcar window (e.g., 60 s), where $i = 0$ is at 09:40:00 UT such that $i = -60/2$ represents the W and J values at 09:39:30 UT and $i = 60/2$ represents the W and J values at 09:40:30 UT, for example,

Because THEMIS does provide time-dependent values at a 3 s cadence (Figure 1a), our future study will incorporate actual values over time, for example, from 09:00–11:00 UT. Because this will require significant additional computational time, this initial study simplifies the time-dependence by applying the boxcar averages instead. Figure 2, discussed in the next section, displays the energy flux and mean energies for these boxcar averages at 09:40 UT in 2D.

Note that the two circles of non-zero values that fall outside of the main ASI mosaic, centered around 62° latitude, 225° longitude and 57° latitude, 260° longitude (as seen in the mean energy column), are artifacts of the code and are not real.

3. Electron Thermal Heat Flux Formation

The detailed classification of precipitated to the atmosphere electrons is given by Newell et al. (2009) and McIntosh & Anderson (2014). McIntosh & Anderson used 8 years of electron precipitation data from the Defense Meteorological Satellite Program to categorize 30 million spectra as either diffuse or accelerated: with 47.05% being best fit with Maxwellian distributions (diffuse), 31.37% kappa distributions, 12.20% as monoenergetic, and 9.38% as broadband (the latter 3 are accelerated). As demonstrated by Khazanov, Sibeck, and Chu (2021), the height integrated ionospheric conductance is very sensitive to the shape of precipitated electron distribution function. Now we demonstrate this effect for the calculation of the electron heat fluxes using the most observed (according to McIntosh & Anderson (2014)) electron distribution functions in aurora:

$$\Phi(E) = AE\exp\left(-\frac{E}{E_0}\right) \quad (2)$$

$$\Phi(E) = AE\left(1 + \frac{E}{\kappa E_0}\right)^{-\kappa-1} \quad (3)$$

$$\Phi(E) = A\exp\left(-\frac{(E-E_0)^2}{2\sigma^2}\right) \quad (4)$$

which are Maxwellian (1), Kappa (2), and Gaussian (3) distribution functions, correspondingly. $\Phi(E)$, E_0, A, and σ are differential number flux, auroral characteristic energy, normalization constant, and $\sigma = 0.1E_0$ (Banks et al., 1974), respectively.

Follow up to the methodology of heat flux calculation presented in Figure 1g in the region of diffuse (Khazanov et al., 2020) and discrete (Khazanov et al., 2021b) auroras, Figure 1h generalizes electron heat fluxes results presented in these papers on the range of characteristic energies from 400 eV to 10 keV. To use these relations, we must connect the average energy of the precipitation provided by the observations with the characteristic energy used by the theoretical calculation to define the thermal flux. Figure 1i shows how the mean and characteristic energies are connected for different distribution functions when accounting multiple electron atmospheric backscatter/reflections using the methodology and results of (Khazanov, Sibeck, & Chu, 2021; Khazanov et al., 2018). Figure 1h clearly demonstrate the sensitivities of different shapes of electron distribution functions (Equations 2–4) in calculating the thermal electron fluxes. It should be noted that Figure 1h was calculated with different normalization constants A that provide *identical* energy fluxes of precipitated electrons of 1 erg $\cdot$ cm^{-2} $\cdot$ s^{-1}. The only commonality in the results presented in Figure 1h are decreasing electron thermal fluxes with increasing characteristic energies (Equations 1–3). Such a dependence comes from the decrease of the intensity of the secondary electrons (with grows of E_0) escaping to the magnetosphere where they degrade and form the electron heat flux (Khazanov et al., 2014).

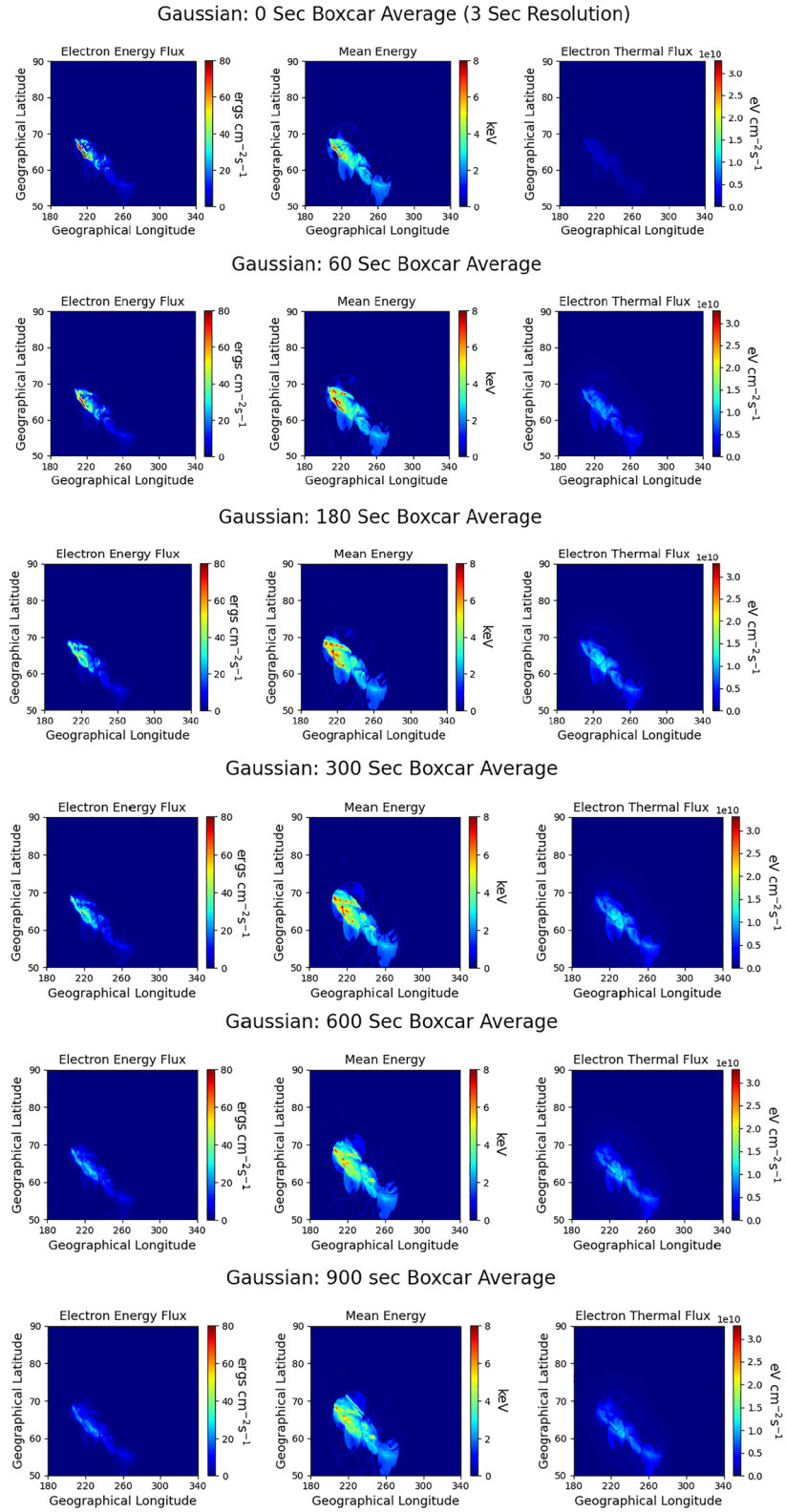

Figure 2. Electron heat flux development (the third column) depending on different temporal boxcar averages to the data centered at 09:40 UT using Gaussian electron distribution functions for precipitated electrons: first column shows energy fluxes of precipitated electrons, and the second one corresponding mean energies.

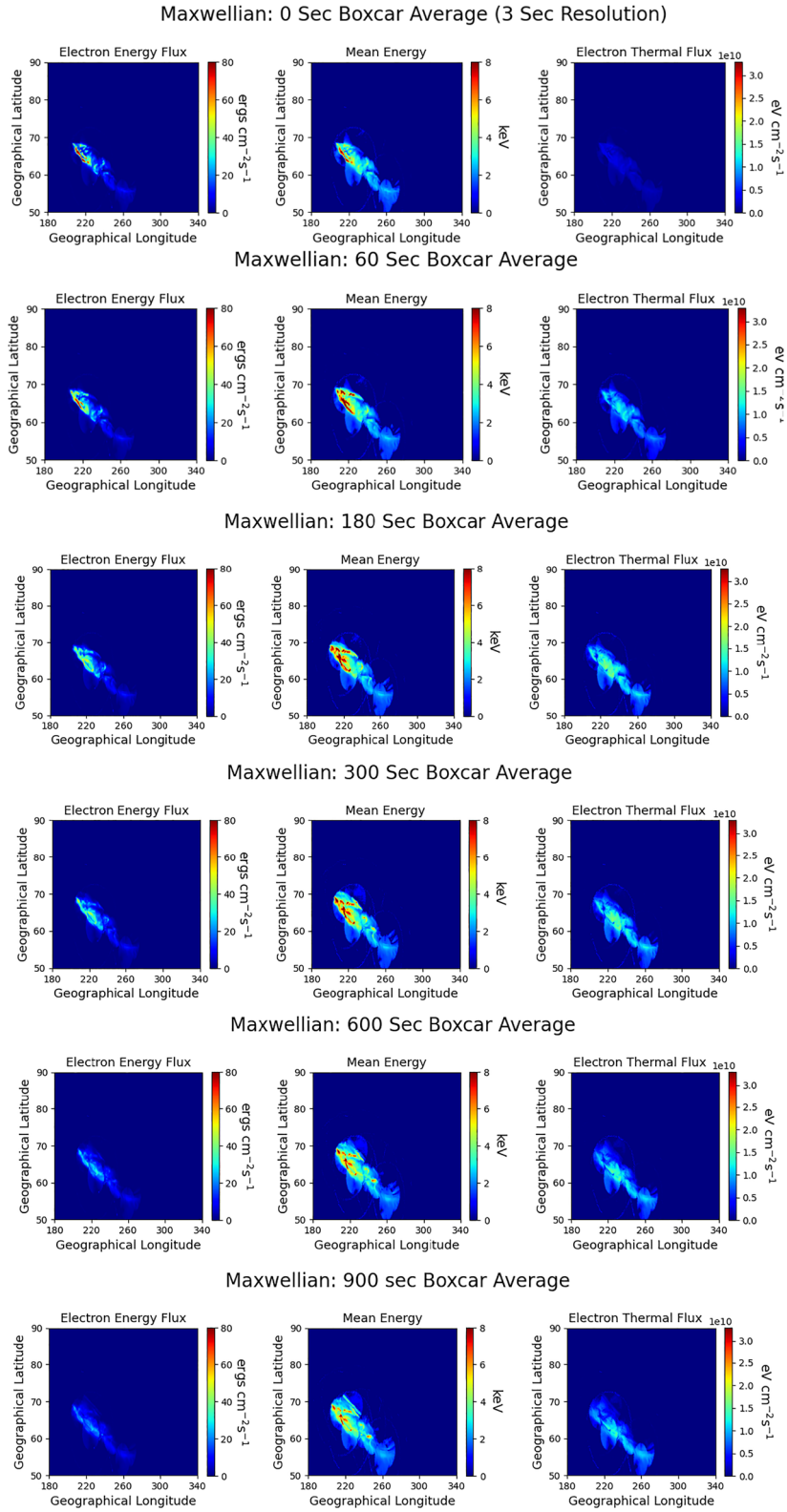

Figure 3. Electron heat flux development (the third column) depending on different temporal boxcar averages to the data centered at 09:40 UT using Maxwellian electron distribution functions for precipitated electrons: first column shows energy fluxes of precipitated electrons, and the second one corresponding mean energies.

Figure 1j presents the non-steady state development of electron heat flux using different characteristic energies for each distribution and different distribution shapes of electron precipitated fluxes. The Gaussian distribution function was selected with characteristic energy of 1 keV, the Kappa distribution function with $\kappa = 3.5$ and $E_0 = 2$ keV, and Maxwellian distribution with $E_0 = 3$ keV. The only common feature in all these functions was the selection of the normalization constants A to provide for all cases *identical* energy fluxes, 1 erg $\cdot$ cm^{-2} $\cdot$ s^{-1}. Analyzing Figure 1j one can see almost identical time scale development of electron heat fluxes when they transition to the steady state conditions around 100 s. Apparently, this phenomenon relates to the fact that below ~100 eV, the secondary electron distribution *shapes* are close to each other and do not depend on the distribution function of their sources (2)–(4).

STET simulations presented in Figures 1h–1j are important intermediate steps that are based on a very time-consuming kinetic calculations and serve as the connector between the THEMIS ASI data and electron heat flux calculation. These simple relations, *for the first time*, connect auroral electron precipitated events with heat flux calculation and represents our newly developed STET-based model.

4. Results and Discussion

As discussed in Section 2, Gabrielse et al. (2021) described a new method that estimates the auroral scale sizes of intense precipitating electron energy fluxes and their mean energies using THEMIS ASI data. They applied this technique to evaluate precipitated electron energy flux and average energy for two substorms, presenting a mosaic of these parameters across Canada and Alaska and validated their results using PFISR observations.

The kaleidoscope of lights and their time variations in the aurora is required to examine the dynamics of the mesoscale heat flux formation. In this analysis we use the results of the calculation presented in Section 3 and Figure 1j. As Figure 1j shows, it takes approximately 5 min to develop the steady-state heat flux solution. If, however, precipitation lasts for a shorter time period, a corresponding time-dependent correction must be taken into account. The THEMIS ASI data presented by Gabrielse et al. (2021) were time synchronized with a 3 s cadence. This allows for the study of electron precipitation in a wide time-dependent range of auroral variation with multiple spatial and temporal scales.

Figures 2 and 3 present 2D electron energy fluxes (first column), the mean energies (second column), and corresponding electron heat fluxes (third column) for 2010-02-16 at 09:40:00 UT for various boxcar averages of the ASI data over time: 0 (no averaging done), 60, 180, 360, 600, and 900 s. We perform the boxcar averages because the heat flux value depends on the conditions leading up to the time of interest. As discussed in Section 2, we assume the average value at 09:40 UT is constant for the duration of the average (e.g., 60, 180, etc.) and calculate the heat flux over that duration. This method mimics the results of an instrument that has lower temporal resolution, e.g., one that integrates the light intensity over 60 s and must find the average for that duration. A future work will utilize the actual time-variable energy fluxes and mean energies provided for these time windows by THEMIS ASI. We then calculate the electron heat flux using the relations presented in Section 3, based on the publications of Khazanov et al. (2020, 2021a). As in Gabrielse et al. (2021), the data in Figures 2 and 3 use assumptions regarding the distribution function of precipitating electrons: Gaussian (Figure 2) and Maxwellian (Figure 3). As was demonstrated by Hecht et al. (2008), the uncertainty involved in this assumption depends on deduced parameters from the optical observation which have errors of 10%–25%. Although Gabrielse et al. (2021) provides the energy fluxes and mean energies for both Maxwellian and Gaussian distributions, they do not distinguish between the types of auroras in their mosaic, which may be a topic of future work.

To see all these variations between different averaging windows, the color bars in Figures 2 and 3 were selected to be the same for each considered parameter. The electron energy fluxes, and mean energies extracted from THEMIS ASI white light observations only slightly depend on the choice of electron distribution function, as seen by the minimal differences in the first two columns between Figures 2 and 3. This is in line with the conclusion by Hecht et al. (2008) about the uncertainty on deducted parameters from the optical observation with errors of 10%–25%. However, as the boxcar average window increases, there are noticeable differences in the energy flux and mean energy: both these parameters decrease with increasing windows, especially for windows >180 s. This is because, as shown in Figures 1a–1f, the temporal variation of the dynamic aurora over a specific location is on the order of a minute or two. Therefore, any averaging done for longer time periods will greatly wash out the peaks in energy flux and mean energy.

The behavior of the calculated electron heat fluxes is more complicated and needs to be explained using the heat flux formation analysis presented in Section 3. As shown in Figure 1j and discussed in Section 3, it takes about 5 min to form a steady state electron heat flux, and the transition time to steady state does not depend on the shape of the distribution function (Equations 1–3). That is why, for both Gaussian and Maxwellian electron distribution functions and boxcar averaging windows of 0, 60, and 180 s such a time delay must be considered. This is done assuming that the start time of the heat flux formation is the beginning of integration time window, "0" secs, and continues for the duration of the window. In the results presented in the third columns in Figures 2 and 3, these assumptions are considered. Note that for the first row in Figures 2 and 3, no boxcar average was applied to the input data; however, the heat flux was calculated over a timeframe of 3 s under the assumption that the energy flux and mean energy remain constant for 3 s (the time resolution of the ASIs). We point out that in Figures 2 and 3, the energy flux for the 3-s boxcar average is the largest but the thermal flux is the smallest. It is because 9:40 UT is the beginning of the substorm, and the energy flux has only been applied over a short time period. As shown in Figure 1, the thermal flux has a long response time, and the energy flux should be applied over a long duration to see substantial thermal flux. The thermal flux for the longer boxcar averages is larger because the energy flux has been applied over a long time due to the averaging.

This general tendency of the electron heat flux intensity to increase with increased boxcar average window lengths is true for both Gaussian and Maxwellian electron distribution functions. Such a growth is easy to explain for the averaging windows of 0, 60, and 180 s because it relates to the transition of electron thermal fluxes to the steady state conditions that it is shown in Figure 1j. There is little change between the energy flux and mean energies from 180 to 300 s, and there is also little change in the heat flux even though the integration time has increased by 120 s. Again, this is because the heat flux has reached steady state as shown in Figure 1j. At 600 and 900 s, the energy flux and mean energies slightly decrease from 300 s, and we also see a slight decrease in heat flux. Because heat flux should increase when mean energy decreases, the slight heat flux decrease at 600 and 900 s demonstrates the role the decreasing energy flux plays in heat flux calculation.

As a tangential though important point, these results demonstrate the large effect that input resolution has on determining heat flux in the system, especially during dynamic events that rapidly change and often occur on mesoscales (<500 km). An aurora with large mean energies and energy fluxes that only exists at a specific location for 60 s (e.g., Figure 2 second row where mean energies are large (red)) has less effect on the heat flux than smaller mean energies and energy fluxes from an aurora that sits at the same location for 300 s (e.g., Figure 2 4th row where mean energies are smaller (green). Incorporating the high-time resolution that THEMIS data provides is a topic of our future work.

Because the ASI data overlaps that of the PFISR facility, we attempted to validate the heat flux methodology presented above with PFISR Te observations. Based on results presented in Figures 2 and 3, we estimate the heat flux variation over PFISR in the range of 10^9–$2\text{-}3 \cdot 10^{10}$ eV $\cdot$ cm$^{-2} \cdot$ s^{-1}. Such heat fluxes can create thermal electron temperature, Te, variations between about 2,500 and 7000 K which should be observable by PFISR if these heat fluxes are steady-state at least for several hours (Khazanov, 2010). Unfortunately for this event, the PFISR data collection mode was not ideal for determining the Te profile; however, in the Supporting Information S1 we use the data (albeit with large errors and limited to lower altitudes) to compare to Te profiles from our heat flux calculations as a rough check on our heat flux determination. To do this we used 5 hr of mean energy and energy flux data from Gabrielse et al. (2021) at the PFISR location to calculate heat flux. These heat fluxes were used as the upper boundary condition in the Polar Wind Outflow Model (PWOM) code (Glocer et al., 2009, 2012, 2017) to model the Te profile. As we demonstrated in the Supporting Information S1, the modeled Te profile using our heat flux inputs, compared to the available Te profile from PFISR, provides credibility to the heat flux results presented above.

5. Conclusion

To conclude the discussion about the formation of electron heat fluxes we want to connect our analysis with experimental and theoretical studies in the past with the major focus on the ionosphere of high latitudes. As was pointed out by Yau and James (2015), "The high-latitude (auroral and polar) ionosphere is the crossroads of the magnetosphere-ionosphere-thermosphere (MIT) system," and the importance of this region related to the electron thermal flux studies were recognized a long time ago in the theoretical studies by Schunk et al. (1987). Observations of electron temperature by Akebono in the polar wind (Yau et al., 1995), radar measurement measurements

of very high Te at Sondrestrom (Kofman & Wickwar, 1984), and DE 2 satellite measurements (Curtis et al., 1985; Fontheim et al., 1987) are strongly indicative of the necessity of the electron heat fluxes to explain experimental results. The latest theoretical studies also confirmed the need to further analyze the heat flux formation (e.g., Glocer et al., 2011, 2017; Mishin, 2019; Mishin & Streltsov, 2021).

Based on the STET code validated by space plasma observation, we developed a rigorous approach to the calculation of electron heat fluxes reaching the topside ionosphere in various regions including the polar cap (Khazanov et al., 2019), diffuse aurora (Khazanov et al., 2020), and discrete aurora (Khazanov et al., 2021a). We used the approaches presented in these papers to obtain the heat flux in combination with a 2D array of auroral precipitation derived from THEMIS ASI white light observations by Gabrielse et al. (2021), validated by comparison with PFISR data. The white light images provide a mesoscale picture of the auroral scale sizes of intense precipitating electron energy fluxes and their mean energies during back-to-back substorms over Canada and Alaska. The new STET code simulations presented in Figures 1h–1j are important intermediate steps that are based on a very time-consuming kinetic calculations and serve as the connector between the THEMIS ASI data and electron heat flux calculation. These simple relations, *for the first time*, connect observed auroral electron precipitated events with heat flux calculation using our newly developed STET-based model. The resulting combination of observations and theoretical calculation provides a 2D picture of the topside electron heat fluxes over a wide area which are capable to creating strongly elevated electron temperature.

As in Gabrielse et al. (2021) we assume both a Maxwellian and a Gaussian electron distribution function to describe the aurora as diffuse and discrete, respectively. As presented in the first two columns of Figures 2 and 3, such assumptions have little influence on the precipitating electron energy fluxes and their mean energies. The corresponding heat fluxes, however, shown in the third column of these figures, have a noticeable difference depending on the assumed shape of the electron distribution. Figure 1h provides additional details that show the sensitivity of the heat flux calculation on the electron distribution shapes of precipitated electrons. Surprisingly, however, the overall temporal dynamics of the heat flux formation presented in Figure 1j is not very sensitive to the shape of precipitated electron distribution function or their characteristic energies.

In the analysis presented in the Supporting Information S1, we presented a rough check of the electron heat flux calculation discussed in Section 4. The modeled Te profiles were compared with PFISR Te observations. The Supporting Information S1 demonstrates that the proposed methodology for the calculation of the heat flux is reasonable when compared to the observations within the limitations of the data. This supports the credibility of the heat flux results presented in this letter.

Data Availability Statement

The 2D maps of energy flux and mean energy that were used in this paper to calculate the heat flux can be found on the Zenodo data repository here: https://doi.org/10.5281/zenodo.6547041. The PFISR data used in the Supporting Information S1 can be found here: https://data.amisr.com/database/tmp/gabrielse/20100216.001/. The processed PFISR Te and errors in Te, and the THEMIS data at the PFISR location, are located here: https://doi.org/10.5281/zenodo.7067588.

Acknowledgments
G. V. K. was partly supported by NASA HTMS program under award of 80NSSC20K1276, the MARBLE Project, funded by the NASA Living with a Star (LWS) Strategic Capabilities program, and NASA LWS awards 80NSSC19K0080 and 80NSSC21K1552. G.V.K and A.G. acknowledge the award 80NSSC20K1817. C. G. and Y.N. would like to acknowledge the NASA grant 80NSSC20K0725 and the AFOSR Grant FA9559-16-1-0364. The THEMIS mission is supported by NASA contract NAS5-02099, NSF Grant AGS-1004736, and CSA contract 9F007-046101.

References

Banks, P. M., Chappell, C. R., & Nagy, A. F. (1974). A new model for the interaction of auroral electrons with the atmosphere: Spectraldegradation, backscatter, optical emission, and ionization. *Journal of Geophysical Research*, *79*(10), 1459–1470. https://doi.org/10.1029/JA079i010p01459

Bekerat, H. A., Schunk, R. W., & Scherliess, L. (2007). Estimation of the highlatitude topside electron heat flux using DMSP plasma density measurements. *Journal of Atmospheric and Solar-Terrestrial Physics*, *69*(9), 1029–1048. https://doi.org/10.1016/j.jastp.2007.03.015

Curtis, S. A., Hoegy, W. R., Brace, L. H., & Winningham, J. D. (1985). Cusp altitudinal electron temperature gradient: Dynamics explorer 2 implications for heating mechanisms. *Journal of Geophysical Research*, *90*(A5), 4415–4419. https://doi.org/10.1029/ja090ia05p04415

Fallen, C. T., & Watkins, B. J. (2013). Diurnal and seasonal variation of electron heat flux measured with the poker flat incoherent-scatter radar. *Journal of Geophysical Research: Space Physics*, *118*(8), 5327–5332. https://doi.org/10.1002/jgra.50485

Fontheim, E., Brace, L., & Winningham, J. (1987). Properties of low-energy electron precipitation in the cleft during periods of unusually high ambient electron temperatures. *Journal of Geophysical Research*, *12*(A11), 12267. https://doi.org/10.1029/ja092ia11p12267

Gabrielse, C., Nishimura, T., Chen, M., Hecht, J. H., Kaeppler, S. R., Gillies, D. M., et al. (2021). Estimating precipitating energy flux, average energy, and hall auroral conductance from THEMIS all-sky- imagers with focus on mesoscales. *Frontiers in Physiology*, *9*, 744298. https://doi.org/10.3389/fphy.2021.744298

Gillies, D. M., Liang, J., Donovan, E., & Spanswick, E. (2020). The apparent motion of STEVE and the picket fence phenomena. *Geophysical Research Letters*, *47*(20), e2020GL088980. https://doi.org/10.1029/2020GL088980

Glocer, A., Khazanov, G., & Liemohn, M. (2017). Photoelectrons in the quiet polar wind. *Journal of Geophysical Research: Space Physics*, *122*(6), 6708–6726. https://doi.org/10.1002/2017JA024177

Glocer, A., Kitamura, N., Toth, G., & Gombosi, T. (2011). Modeling solar zenith angle effects on the polar wind. *Journal of Geophysical Research*, *117*(A4), A04318. https://doi.org/10.1029/2011JA017136

Glocer, A., Kitamura, N., Toth, G., & Gombosi, T. (2012). Modeling solar zenith angle effects on the polar wind. *Journal of Geophysical Research*, *117*(A4), A04318. https://doi.org/10.1029/2011JA017136

Glocer, A., Toth, G., Gombosi, T., & Welling, D. (2009). Modeling ionospheric outflows and their impact on the magnetosphere, initial results. *Journal of Geophysical Research*, *114*(A5), A05216. https://doi.org/10.1029/2009JA014053

Hecht, J. H., Mulligan, T., Strickland, D. J., Kochenash, A. J., Murayama, Y., Tanaka, Y.-M., et al. (2008). Satellite and ground-based observations of auroral energy deposition and the effects on thermospheric composition during large geomagnetic storms: 1. Great geomagnetic storm of 20 November 2003. *Journal of Geophysical Research*, *113*(A1), A01310. https://doi.org/10.1029/2007JA012365

Khazanov, G. V. (2010). *Kinetic theory of inner magnetospheric plasma* (p. 372). Space science Library.

Khazanov, G. V., Glocer, A., & Chu, M. (2020). The formation of electron heat flux in the region of diffuse aurora. *Journal of Geophysical Research: Space Physics*, *125*(8), e2020JA028175. https://doi.org/10.1029/2020JA028175

Khazanov, G. V., Glocer, A., & Chu, M. (2021a). Electron energy interplay in the geomagnetic trap below the auroral acceleration region. *Journal of Geophysical Research: Space Physics*, *126*(5), e2020JA028811. https://doi.org/10.1029/2020JA028811

Khazanov, G. V., Glocer, A., & Chu, M. (2021b). The precipitated electrons in the region of diffuse aurora driven by ionosphere-thermosphere collisional processes. *Geophysical Research Letters*, *48*(16), e2021GL094583. https://doi.org/10.1029/2021GL094583

Khazanov, G. V., Glocer, A., & Himwich, E. W. (2014). Magnetosphere-ionosphere energy interchange in the electron diffuse aurora. *Journal of Geophysical Research: Space Physics*, *119*(1), 171–184. https://doi.org/10.1002/2013JA019325

Khazanov, G. V., Himwich, E. W., Glocer, A., & Sibeck, D. (2016). The role of multiple atmospheric reflections in the formation of the electron distribution function in the diffuse aurora region. *Auroral Dynamics and Space Weather*, 115–130. https://doi.org/10.1002/9781118978719

Khazanov, G. V., Robinson, R. M., Zesta, E., Sibeck, D. G., Chu, M., & Grubbs, G. A. (2018). Impact of precipitating electrons and magnetosphere-ionosphere coupling processes on ionospheric conductance. *Space Weather*, *16*(7), 829–837. https://doi.org/10.1029/2018SW001837

Khazanov, G. V., Sibeck, D. G., & Chu, M. (2021). Magnetosphere-ionosphere coupling of precipitating electrons and ionospheric conductance, space physics and aeronomy collection volume 2. In R. Maggiolo, N. André, H. Hasegawa, D. T. Welling, Y. Zhang, & L. J. Paxton (Eds.), *Magnetospheres in the solar system, geophysical monograph 259* (1st ed.). John Wiley & Sons, Inc. https://doi.org/10.1002/9781119507512

Khazanov, G. V., Sibeck, D. G., & Zesta, E. (2019). The formation of electron heat flux over the sunlit quiet polar cap ionosphere. *Geophysical Research Letters*, *46*(17–18), 10201–10208. https://doi.org/10.1029/2019GL084522

Kofman, W., & Wickwar, V. B. (1984). Very high electron temperatures in the daytime F region at Sondrestrom. *Geophysical Research Letters*, *11*(9), 919–922. https://doi.org/10.1029/gl011i009p00919

McIntosh, R. C., & Anderson, P. C. (2014). Maps of precipitating electron spectra characterized by Maxwellian and kappa distributions. *Journal of Geophysical Research: Space Physics*, *119*(12), 10116–10132. https://doi.org/10.1002/2014JA020080

Mishin, E., & Streltsov, A. (2019). STEVE and the picket fence: Evidence of feedback-unstable magnetosphere-ionosphere interaction. *Geophysical Research Letters*, *46*(24), 14247–14255. https://doi.org/10.1029/2019GL085446

Mishin, E., & Streltsov, A. (2021). *Nonlinear wave and plasma structures in the auroral and subauroral geospace* (p. 621). Elsevier.

Mishin, E. V. (2019). Artificial aurora experiments and application to natural aurora. *Frontiers in Astronomy and Space Sciences*, *6*. https://doi.org/10.3389/fspas.2019.00014

Newell, P. T., Sotirelis, T., & Wing, S. (2009). Diffuse, monoenergetic, and broadband aurora: The global precipitation budget. *Journal of Geophysical Research*, *114*(A9), A09207. https://doi.org/10.1029/2009JA014326

Nishimura, Y., Deng, Y., Lyons, L. R., McGranaghan, R. M., & Zettergren, M. D. (2021). Multiscale dynamics in the high-latitude ionosphere. In C. Huang, G. Lu, Y. Zhang, & L. J. Paxton (Eds.). *Ionosphere dynamics and applications*. https://doi.org/10.1002/9781119815617.ch3

Richmond, A. D., Ridley, E. C., & Roble, R. G. (1992). A thermosphere/ionosphere general circulation model with coupled electrodynamics. *Geophysical Research Letters*, *19*(6), 601–604. https://doi.org/10.1029/92gl00401

Ridley, A. J., Deng, Y., & Toth, G. (2006). The global ionosphere–thermosphere model. *Journal of Atmospheric and Solar-Terrestrial Physics*, *68*(8), 839–864. https://doi.org/10.1016/j.jastp.2006.01.008

Samara, M., Michell, R. G., & Khazanov, G. V. (2017). First optical observations of interhemispheric electron reflections within pulsating aurora. *Geophysical Research Letters*, *44*(6), 2618–2623. https://doi.org/10.1002/2017GL072794

Schunk, R. W., Sojka, J. J., & Bowline, M. D. (1986). Theoretical study of the electron temperature in the high-latitude ionosphere for solar maximum and winter conditions. *Journal of Geophysical Research*, *91*(A11), 12041–12054. https://doi.org/10.1029/JA091iA11p12041

Schunk, R. W., Sojka, J. J., & Bowline, M. D. (1987). Theoretical study of the electron temperature in the high-latitude ionosphere for solar maximum and winter conditions. *Journal of Geophysical Research*, *91*(A11), 12041–12054. https://doi.org/10.1029/JA091iA11p12041

Strickland, D. J., Book, D. L., Coffey, T. P., & Fedder, J. A. (1976). Transport equation techniques for the deposition of auroral electrons. *Journal of Geophysical Research*, *81*(16), 2755–2764. https://doi.org/10.1029/ja081i016p02755

Strickland, D. J., Daniell, R. E., Jasperse, J. R., & Basu, B. (1993). Transport-theoretic model for the electron-proton-hydrogen atom aurora, 2. Model results. *Journal of Geophysical Research*, *98*(A12), 21533–21548. https://doi.org/10.1029/93JA01645

Yau, A. W., & James, H. G. (2015). CASSIOPE enhanced polar outflow probe (e-POP) mission overview. *Space Science Reviews*, *189*(1–4), 3–14. https://doi.org/10.1007/s11214-015-0135-1

Yau, A. W., Whalen, B. A., Abe, T., Mukai, T., Oyama, K. I., & Chang, T. (1995). Akebono observations ofanisotropy in the polar wind. *Journal of Geophysical Research*, *100*(A9), 17451–17463. https://doi.org/10.1029/95JA00855

References From the Supporting Information

Banks, P. (1966). Charged particle temperatures and electron thermal conductivity in the upper atmosphere. *Annals of Geophysics*, *22*, 557–587.

Dougherty, J. P., & Farley, D. T. (1960). A theory of incoherent scattering of radio waves by a plasma. *Proceedings of the Royal Society of London*, *259*(1296), 79–99.

Kudeki, E., & Milla, M. A. (2011). Incoherent scatter spectral theories—Part I: A general framework and results for small magnetic aspect angles. *IEEE Transactions on Geoscience and Remote Sensing*, *49*(1), 315–328. https://doi.org/10.1109/TGRS.2010.2057252